(3×1)-Br/Pt(110) structure and the charge-density-wave-assisted $c(2\times2)$ to (3×1) phase transition

C. Deisl, K. Swamy, N. Memmel, and E. Bertel
Institut für Physikalische Chemie, Unversität Innsbruck, Innrain 52a, A-6020 Innsbruck, Austria

C. Franchini,* G. Schneider, and J. Redinger
Institut für Allgemeine Physik and Center for Computational Materials Science, Vienna University of Technology, Getreidemarkt 9/134, A-1060 Vienna, Austria

S. Walter, L. Hammer, and K. Heinz
Lehrstuhl für Festkörperphysik, Institut für Angewandte Physik, Staudtstr. 7-A3, D-91058 Erlangen, Germany
(Received 3 September 2003; revised manuscript received 25 November 2003; published 6 May 2004)

After our recent report on the formation of a (3×1) charge-density-wave phase in the quasi-one-dimensional system Br/Pt(110) we present a detailed investigation of the $c(2\times2)\Rightarrow(3\times1)$ transition in the Br/Pt(110) adsorption system. This includes the atomic structure of the (3×1) phase as determined by quantitative low-energy electron diffraction (LEED) and density functional theory calculations. While in the parent $c(2\times2)$ phase with coverage $\Theta=1/2$ ML the Br atoms occupy every second short-bridge site on the unreconstructed (1×1)-Pt(110) surface, the adatoms in the (3×1) phase at coverage $\Theta=2/3$ ML reside in every third short-bridge and long-bridge sites. Charge densities and vertical relaxations of the Pt atoms forming the short- and long-bridge sites are different, thus yielding a modulation of both, the charge and the position of the outermost Pt atoms with a period of three nearest-neighbor spacings. For 1/2 ML$<\Theta\leqslant$0.58 ML LEED intensity and scanning tunneling microscope (STM) measurements reveal the nucleation of (3×1) islands surrounded by areas with a local coverage of 1/2 ML. Within the latter areas the STM measurements indicate dynamical fluctuations of the Br positions at room temperature. In the time average every short-bridge site is sampled by the mobile Br atoms, but in the neighborhood of (3×1) islands every third short-bridge site seems to be preferentially occupied.

DOI: 10.1103/PhysRevB.69.195405 PACS number(s): 68.43.Fg, 61.14.Hg, 68.43.Bc, 68.37.Ef

I. INTRODUCTION

Low-dimensional systems own an extraordinary potential in materials design and development. This is due to the fact that their ground state is the result of a delicate balance between various interactions. Individual microscopic control of these interactions allows to switch between different phases or eventually tune the material's macroscopic properties in a quasicontinuous way.[1–3] One of these interactions is the $2k_F$ electron-phonon interaction which, due to the divergence of the response function $\chi(2k_F)$ at $T=0$ K in one-dimensional systems, can give rise to a Peierls transition into a charge-density-wave (CDW) phase.[4] The periodicity of the resulting CDW can in principle be continuously tuned.[5] In real systems more complex patterns may evolve due to soliton formation.[3,6,7]

Recently, we reported on the observation of a CDW phase in the adsorption system Br/Pt(110) (Ref. 8) lacking, however, the precise atomic structure for both the CDW and the undistorted parental phase. Meanwhile, the latter has been identified as a $c(2\times2)$-Br/Pt(110) adsorption phase [Fig. 1(a)] with Br atoms at coverage $\Theta=1/2$ residing in every second short-bridge site along the close-packed atomic rows of the unreconstructed Pt(110) substrate.[9] Atomic positions derived from low-energy electron diffraction (LEED) intensity data and density-functional theory (DFT) calculations agreed to a precision of better than 3 pm. The present work reports a similarly precise determination of the (3×1) phase [Fig. 1(b)] obtained for the ideal coverage $\Theta=2/3$ ML. Additionally, we offer an investigation of the transition from the $c(2\times2)$ to the (3×1) phase by LEED intensity and room-temperature scanning tunneling microscope (STM) measurements. We show that the (3×1) CDW phase is associated with a soft mode of the Rayleigh phonon. The transition into the (3×1) phase apparently involves long-range fluctuations at finite temperature and can be triggered by a variety of different adparticles. While experimental data suggest that the phase transition is caused by a CDW, DFT calculations yield a substantially higher energy for the (3×1) phase. This would indicate that the CDW is only accompanying but not driving the phase transition. A complete experimental determination of the energetics of the phase transition is not possible on the basis of quantitative LEED and room-temperature STM investigations alone. Temperature-variable STM measurements planned for the near future should provide the complementary information required to solve the puzzle.

II. EXPERIMENTAL AND COMPUTATIONAL DETAILS

The experimental and computational details are much the same as described previously for the investigation of the $c(2\times2)$ phase,[9] so that a brief résumé is sufficient. All experiments were carried out in an ultrahigh vacuum system with base pressure $<8\times10^{-11}$ mbar. Bromine was dosed

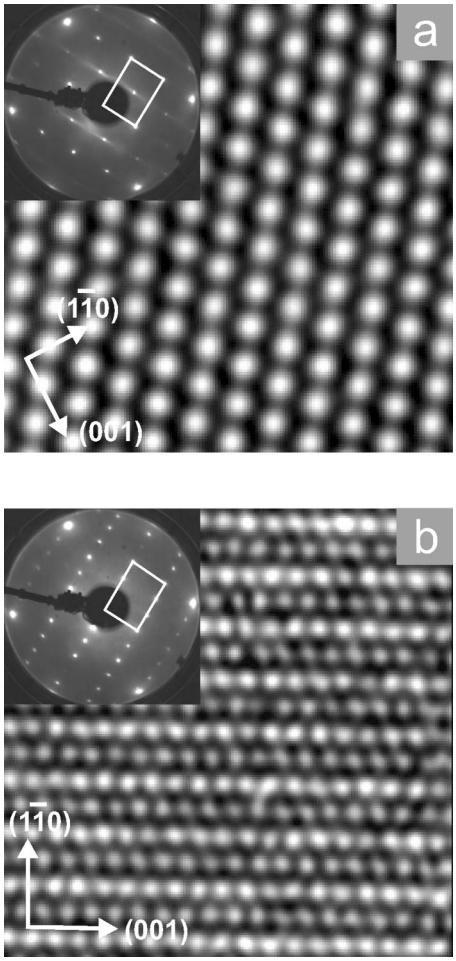

FIG. 1. (a) Constant-current STM image (0.82 V, 1.14 nA; 50 $\times 50$ Å^2) and LEED pattern ($E=147$ eV) of the $c(2\times2)$ phase with a Br coverage of 0.5 ML. (b) Constant-current image (12 mV, 0.63 nA; 70×70 Å^2) and LEED pattern ($E=147$ eV) of a global (3×1) phase with 0.58 ML Br.

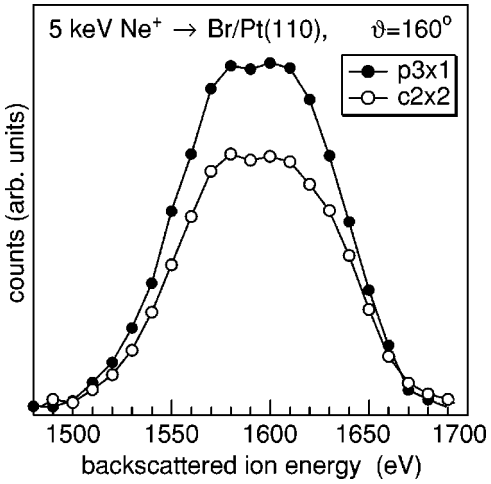

FIG. 2. Energy distribution of Ne^+ ions backscattered ($\vartheta=160°$) from Br/Pt(110). The primary beam was adjusted normal to the surface, its energy was 5 keV.

from a solid-state electrolysis cell. The (3×1) structure [Fig. 1(b)] could be prepared in three different ways monitored by room-temperature STM in the constant-current mode by a commercial STM.[11] The bias voltages quoted in the figure captions of the STM images refer to sample bias. We always started with the perfect $c(2\times2)$ phase [Fig. 1(a)]. Then at about 190 K either (i) a small or (ii) a rather large additional amount of Br was deposited with most of the latter subsequently removed by thermal desorption at temperatures 670–740 K. Alternatively, preparation (iii) consisted of the adsorption of small amounts of CO or NO on the $c(2\times2)$ phase, whereby the actual coverage was determined using the exposure time and the sticking coefficient available from a temperature programmed desorption (TPD) study.[10]

Preparation (i) deserves to be described in some more detail. When only little additional Br is to be added there is a substantial uncertainty due to the difficulty to reach steady-state conditions for electrolysis, transport, and desorption of Br in the cell. The time to reach steady state is large compared to the exposure time for adding only small Br doses. In order to obtain a reliable calibration, low-energy Ne^+ ion scattering experiments were carried out. Figure 2 displays the energy distribution of 5 keV Ne^+ ions backscattered from optimally prepared $c(2\times2)$ and (3×1)-Br/Pt(110) phases. Hereby, ''optimally prepared'' refers to maximum intensities of the fractional order LEED spots in each phase. The ion signal in Fig. 2 is due to Ne^+ ions elastically scattered from Br atoms. Its area is directly proportional to the number density of Br atoms on the surface. The ratio of the signal areas for the two phases is $1.33(\pm0.07)$. With input of the 1/2 ML coverage of the $c(2\times2)$ phase as derived from our earlier quantitative structure determination,[9] the coverage for an optimally developed (3×1) phase is obtained as 0.665 ML. This fits to the ideal coverage $\Theta_{id}=2/3$ ML of the (3×1) phase determined in the present work and thus additionally confirms the structural model. The exposures applied to induce the transition from the $c(2\times2)$ to the (3×1) phase are derived from these calibration points. Despite our efforts, we estimate that the uncertainty of the figures quoted for the additional coverage (i.e., $\Delta\Theta=\Theta-0.5$ ML) amounts to about 20%.

LEED intensity data were recorded using a charge-coupled device camera operated under computer control (AIDA-PC) (Ref. 12) allowing for both spatial spot profile measurements and the measurement of spot integrated data leading to $I(E)$ spectra. The latter data were always taken at low temperatures (≈130 K) and in steps of 0.5 eV from 40 to 400 eV for normal incidence of the primary beam. In contrast, spot profiles were recorded at ≈370 K in order to follow the structural transition $c(2\times2)\Rightarrow(3\times1)$.

For the retrieval of structural data from the measured $I(E)$ spectra the perturbation method tensor LEED (Refs. 12,13) was applied using the TENSERLEED program package[14] to which 14 relativistically calculated and spin averaged phase shifts for Pt and Br were input. An energy dependent real and imaginary part of the inner potential was used as given below. For the structural search a frustrated annealing procedure was used[15] guided by the Pendry R factor[16] for the quantitative comparison of experimental and computed spec-

tra. The variance of the latter was applied for the error estimation.

First-principles DFT calculations were performed using two state-of-the-art methods, the all-electron full-potential linearized augmented plane-wave (FLAPW) method,[17] and the Vienna *ab initio* simulation Package (VASP) (Ref. 18) with the projector augmented wave[19] scheme as implemented by Kresse and Joubert.[20] As in our previous paper[9] two DFT potential approximations have been used: the generalized gradient approximation (GGA) according to Perdew and Wang (PW91) (Ref. 21) and the local density approximation (LDA) in the Perdew-Zunger (Ceperly-Alder) parametrization scheme.[22] A slab of up to 11 layers thickness, repeated along the surface normal for VASP, and a single slab with vacuum on both sides for FLAPW served as a surface model. In VASP the repeated slabs are separated by a vacuum layer of at least 9.5 Å thickness.

In FLAPW calculations a symmetric (with respect to the middle layer) nine layer Pt slab with additional Br atoms on both sides was used. Br atoms and four Pt layers were allowed to relax. Well-converged results were obtained for plane-wave cutoff $k_{max}=3.7$ a.u. Inside the muffin-tin spheres, the angular momentum expansion was taken up to $\ell_{max}=8$, both for the full-potential and charge-density representations. The core electrons, including the $5p$ states for Pt, were treated fully relativistically and the valence electrons derived from the atomic $5d$, $6s$, and $6p$ Pt orbitals and $4s$, $4p$ Br orbitals are treated semirelativistically, i.e., dropping only the spin-orbit term in the Hamiltonian. All the FLAPW results have been obtained using a Cunningham[23] type *k*-mesh of nine special points in the irreducible wedge of the strictly two-dimensional Brillouin zone.

For the VASP calculations an energy cutoff of about 230 eV and a $6\times6\times1$ Monkhorst-Pack type *k*-point mesh was sufficiently accurate for the present purposes. Calculations have been performed for a 11 layers Pt substrate slab with an adlayer of Br atoms on one side. All layers were relaxed except four layers of the Pt substrate on the far side which had been frozen to bulk geometry. Such a setup allowed not only a highly accurate determination of the relaxation in the adlayer substrate complex but also for layers deeper in the bulk which turned out to be non-negligible. For both methods, the geometry was optimized until all forces were smaller than 0.01 eV/Å.

III. THE STRUCTURE OF THE (3×1)-Br/Pt(110) PHASE

A. LEED analysis

The accumulated data base width of intensities recorded for the (3×1) phase in the energy range 40–400 eV amounts to $\Delta E_i=2325$ eV and $\Delta E_f=3375$ eV for integer and fractional order beams, respectively, giving a rather large total of $\Delta E=5700$ eV. The real part of the inner potential was allowed to vary with energy[24] according to $V_{0r}=V_{00}+\max(-10.63,0.47-81.37/(E/\mathrm{eV}+13.97)^{1/2})$ eV with V_{00} determined in the course of the theory-experiment fit ($V_{00}=-0.5$ eV). The imaginary part describing the electron attenuation was also made energy dependent according to $V_{0i}=6(E/(230\ \mathrm{eV}+V_{0r}))^{1/3}$ eV.

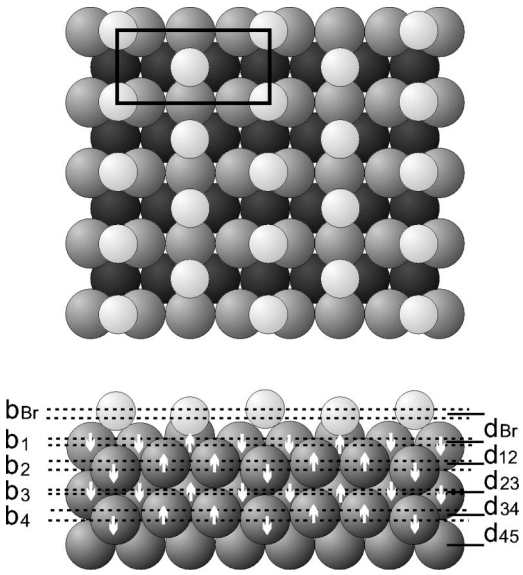

FIG. 3. Model of the (3×1)-Br/Pt(110) phase with structural parameters determined. Interlayer spacings d_{ij} refer to the center-of-mass planes of layers *i* and *j*. Adsorbate induced movements of substrate atoms leading to the buckling of layer *i* with amplitude b_i are indicated by arrows.

With the (3×1) phase best developed at coverage 2/3 and with the additional information from the STM images (see below) the structural model must be according to Fig. 3 with Br adatoms residing in long- and short-bridge sites of the unreconstructed substrate [one should note that the missing row reconstruction of uncovered Pt(110) had already been lifted in the $c(2\times2)$ phase[9]]. With the two adsorption sites being inequivalent this is a (3×1) structure with two atoms per unit cell rather than a $c(3\times1)$ structure. Consequently, the corresponding Br adsorption heights can be different equivalent to a buckled adlayer, which was considered by the fit parameter b_{Br}. This buckling may also involve atomic movements within the substrate, so that a layer dependent buckling with amplitudes b_i in substrate layer *i* had to be considered as also indicated in Fig. 3. Additionally, the interlayer spacings d_{Br} and $d_{i,i+1}$, which in the following are given with respect to the center of mass planes of layers, entered the analysis. Also, isotropic thermal vibrations v_{Br} for Br atoms and v_1 for top layer Pt atoms were included as fit parameters, while the vibrational amplitude of bulk Pt atoms was fixed at $v_b=0.07$ Å according to the bulk Debye temperature. With bucklings and layer spacings up to $i_{max}=4$ and with two vibrational amplitudes considered, there was a total of $n=12$ parameters to be determined. With the estimation that every peak in a spectrum provides an independent piece of structural information and by the fact that the peak width is about $4V_{0i}\approx20$ eV, the number of independent information is $N=\Delta E/4V_{0i}\approx280$. Compared to $n=12$ this is equivalent to a huge redundancy factor putting our analysis on rather safe statistical grounds.

The structural search converged rapidly producing a minimum Pendry *R* factor of $R_P=0.22$ which is of about the same level of theory-experiment agreement as had been reached for the $c(2\times2)$ phase [$R_P=0.23$ (Ref. 9)]. The vari-

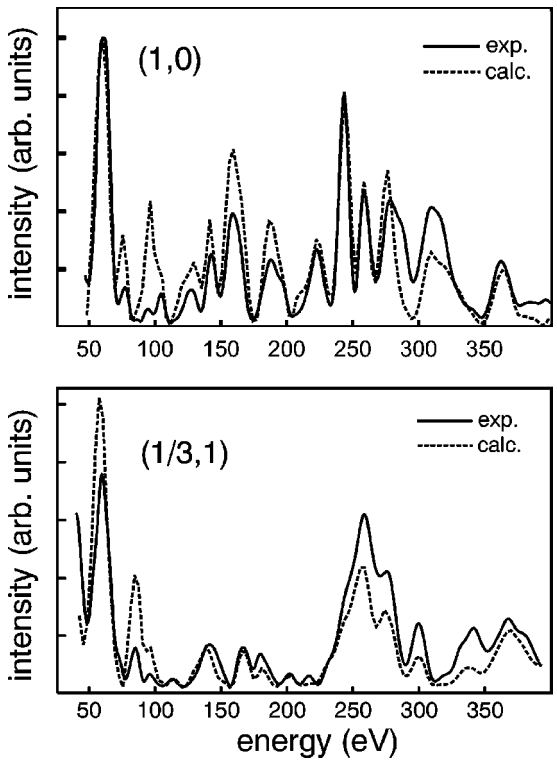

FIG. 4. Comparison of experimental and calculated best-fit spectra for (3×1)-Br/Pt(110) for a selected integer and fractional order beam.

ance of the R factor is $\mathrm{var}(R_P)=R_P\sqrt{2/N}\approx0.02$ from which error limits of about 0.02 Å for layer spacings and about 0.03 Å for buckling amplitudes are estimated (neglecting possible correlations as usual). Consistent with the R-factor level, the visual comparison of experimental and best-fit calculated spectra is favorable, too, as demonstrated for two selected beams in Fig. 4. We also mention that the ratio between the energy averaged intensity levels of fractional and integer order spectra is $r_{th}=0.82$ in theory compared to the experimental value $r_{expt}=0.55$. This is fair agreement in view of the fact that the calculated value must be always higher because of the ideal order assumed.

The quantitative values for the model parameters as described in Fig. 3 and the Br-Pt bond lengths calculated from them are given in Table I. They are compared to the DFT results to be described in the following section and we postpone the discussion of the results to after that.

B. DFT Analysis

Stimulated by our previous results for the $c(2\times2)$ Br phase we performed DFT calculations using, as described in Sec. II an almost identical setup. The stability of particular adsorption sites as determined by the average adsorption energy per Br atom for the $c(2\times2)$ phase and the experimental STM data—assuming the Br atoms to appear as protrusions—hinted towards a structure with both short and long bridges occupied. The optimum relaxed geometry for the (3×1) structure using different theoretical methods and exchange-correlation potentials is given in Table I. It is interesting to note that in accordance with the $c(2\times2)$ structure, most of the mean interlayer spacings are found near the bulk value. In particular, these relaxations are much smaller than bucklings within the layers, which are quite large even in the second Pt layer below the Br adsorbate. The strong buckling of the first and even the second substrate layer may be interpreted as a frozen Rayleigh phonon providing the periodic lattice distortion for the CDW phase. On the other hand, it appears as a compromise for maintaining the optimum Br-Pt bond length without introducing too much corrugation into the Br layer. This can be inferred by comparing the bond lengths for the short-bridge L_S and the long-bridge positions L_L, respectively. Not unexpectedly, these values are also close to those obtained for the $c(2\times2)$ phase.[9] The same is true for lateral pairings of the Pt substrate, which never exceed 0.02 Å. Again similar to $c(2\times2)$,[9] the internal differences between VASP and FLAPW results are within the experimental error limits except for the bucklings b_1 and b_2 which are smaller for FLAPW. We attribute this to the different thickness and symmetry of the slab (11 layer asymmetric vs nine layer symmetric). Larger differences are found for the Br-Pt(110) distance depending on whether LDA or GGA potentials are used. Compared to GGA, the tendency of LDA to overbind leads to smaller values of d_{Br} by 0.07–0.08 Å, clearly exceeding the experimental error margin of ±0.02 Å.

TABLE I. LEED and DFT (VASP-GGA, VASP-LDA, FLAPW-LDA) results for the (3×1)-Br/Pt(110) phase with d_{Br} the spacing between the center-of-mass planes of the Br and top substrate layer, $\Delta d_{i,i+1}$ the changes of the substrate interlayer spacings compared to the respective bulk value and referring again to the respective center-of-mass planes. The quantities b_{Br} and b_i denote the vertical buckling amplitudes in the different layers according to Fig. 3. L_S and L_L are the Br-Pt bond lengths in the short- and long-bridge sites, respectively. All values are in Å. The error limits of the LEED analysis amount to about ±0.02 Å for layer spacings and ±0.03 Å for buckling amplitudes.

	d_{Br}	L_S	L_L	Δd_{12}	Δd_{23}	Δd_{34}	Δd_{34}	d_0	b_{Br}	b_1	b_2	b_3	b_4
LEED	1.91	2.53	2.54	−0.09	+0.00	+0.04	−0.01	1.387	0.26	0.25	0.10	0.01	0.04
VASP-GGA	1.89	2.51	2.57	−0.05	+0.01	+0.02	−0.01	1.409	0.24	0.22	0.11	0.02	0.04
VASP-LDA	1.84	2.45	2.51	−0.06	+0.01	+0.01	−0.01	1.382	0.25	0.21	0.10	0.02	0.02
FLAPW-LDA	1.83	2.45	2.52	−0.06	+0.01	+0.01	−0.01	1.378	0.28	0.15	0.05	0.00	0.02

Keeping in mind the arguments above, we chose the calculation for the thicker slab and GGA potentials (VASP-GGA) as a reference—denoted DFT—throughout this work.

C. Discussion

For the structural parameters determined and the resulting Br-Pt bond lengths for the (3×1) phase there is an impressive agreement between the LEED results and the DFT calculations. For most parameters the discrepancies are much below 0.05 Å, very similar to our recent results for $c(2\times2)$-Br/Pt(110) (Ref. 9) (actually, in our reference DFT calculation only Δd_{12} is slightly outside the experimental error bars). Due to the two inequivalent adsorption sites (long and short bridges), the adsorption heights of the respective Br atoms are different, equivalent to a buckling of the adlayer by as much as 0.24/0.26 Å (LEED/DFT values, respectively). As chemically reasonable, the corresponding Br-Pt bond lengths (L_L and L_S, respectively) differ only slightly (see Table I) in experiment, while the calculated difference is about 2%. The experimental values for L_S and L_L are slightly larger than the short-bridge bond length determined for the $c(2\times2)$ phase (2.47 Å).[9] Similarly, in the calculations L_L is also larger, while L_S is the same as calculated for the $c(2\times2)$ structure (2.51 Å). Such similar bond lengths are accomplished by sharing the buckling with substrate layers. A substantial amplitude of 0.25/0.22 Å (LEED/DFT) is found in the top Pt layer. It only gradually vanishes when going deeper into the surface. As indicated by the arrows in Fig. 3, the atomic buckling shifts in the Br and top Pt layer are in opposite directions for the atoms involved in the two adsorption sites, thus reducing the buckling.

Turning now to the adsorption energies, we find a value of 6.14 eV per (3×1) unit cell, i.e., a mean value of 3.07 eV per Br atom. This has to be compared to the numbers for the $c(2\times2)$ phase, which we recalculated using the same VASP-GGA setup, whereby 3.25 eV and 3.11 eV per Br atom resulted for the short- and long-bridge sites, respectively (in Ref. 9 a slightly different setup was used, so the numbers differ from there slightly, too). From our previous work we learned that a $c(2\times2)$ and (2×1) phase are almost degenerate in energy, which means that there is almost no energy penalty for a registry shift of the short-bridge Br chain. Therefore, we may assume that the adsorption energy for a Br atom in a short-bridge site of the (3×1) phase is the same as for $c(2\times2)$, and estimate a cost of $(2\times3.25-6.14)$ eV$=0.36$ eV for transferring a Br atom from the short-bridge site in the $c(2\times2)$ Br phase to the long-bridge site in the (3×1) structure. This is a large value in view of the only 0.14 eV difference between the two sites for the $c(2\times2)$ phase, so that the Br-Br repulsion across the chains for Br atoms residing in long-bridge sites must be much larger than for short-bridge sites. Since these energetics play an important role in the stability of phases, we will discuss this issue in the following in terms of site energies and mutual repulsions.

For the discussion we chose adsorption models as shown in Figs. 5 and 6 with a $(3\times n)$ cell, i.e. with threefold periodicity along the close-packed Pt rows. The site energies

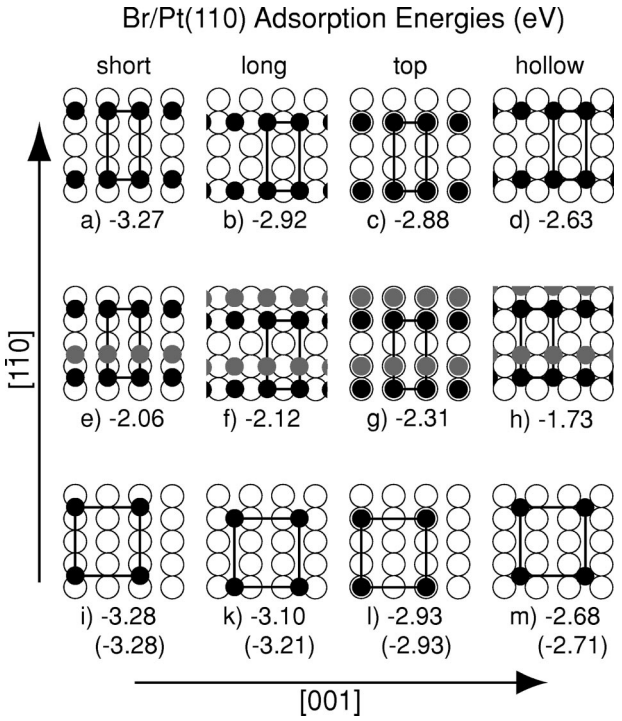

FIG. 5. Adsorption energies per Br atom for various sites (short-bridge, long-bridge, top, and hollow) and arrangements with threefold periodicity along the close-packed Pt rows. Empty circles denote the top layer (1×1) Pt atoms and Br atoms are represented by filled black and gray circles. For arrangements (e)–(h) the energies are given for the additional Br atoms (gray). The values given in parentheses reflect the change when the substrate is allowed to relax also along the [001] direction [which is not possible for (3×1) cells].

denote the energy gain upon adsorption of a single Br atom (chain), while the repulsions are a measure of the cost in energy when two or more Br atoms (chains) approach each other. The main conclusions concerning site energies, barriers, and repulsions drawn from the energies given in Figs. 5 and 6 are the following.

(a) *Site energies* t_{site}. The sequence of relative stabilities for chains of Br atoms adsorbed in the various adsorption sites in a $p(3\times1)$ structure [see Figs. 5(a)–5(d)] are the same as for the $c(2\times2)$ phase.[9] The energy t_{short} for a $p(3\times1)$ short-bridge site is only $(3.27-3.25)$ eV $=0.02$ eV lower than the corresponding value for a $c(2\times2)$ phase, so that Br atoms (chains) separated by two or more short-bridge sites may be considered as noninteracting along the Pt rows. In contrast, for the corresponding energy t_{long} for the long-bridge site we find a value of considerably smaller modulus for the $p(3\times1)$ than for the $c(2\times2)$ structure (-2.92 eV vs -3.11 eV).[25] This can be attributed to the Br-Br repulsion in [001] direction being larger for the $p(3\times1)$ phase. This attribution is inferred from the configuration shown in Fig. 5(k) which yields an energy of -3.10 eV for Br atoms separated by an empty site along [001] and -3.21 eV when the substrate is relaxed also along the [001] direction [note that lateral relaxations of the surface Pt atoms perpendicular to the chains are not possible for

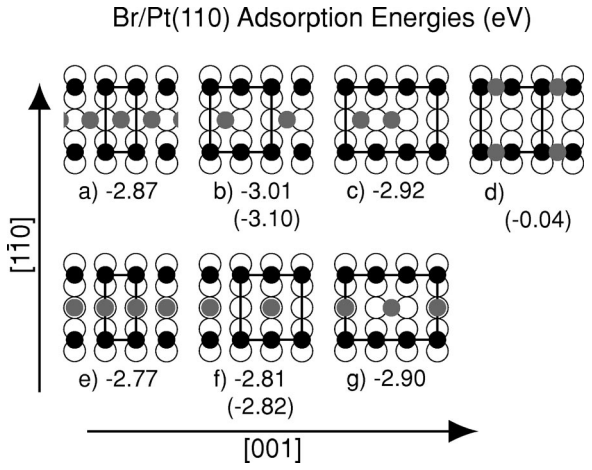

FIG. 6. Adsorption energies of *additional* Br atoms (gray circles) between (3×1) short-bridge Br rows (black circles). Empty circles denote the top layer (1×1) Pt atoms. The values given in parentheses reflect the change when the substrate is allowed to relax also along the [001] direction, not possible for p(3×1) cells. For all arrangements except (d) the black Br atoms are fixed at their ideal p(3×1) short-bridge positions.

$(n\times1)$ structures by symmetry arguments]. Such a behavior is not quite unexpected as t_{long} depends strongly on the formation of the Br-Pt bond at an optimal bond length along [001] which amounts to an energy loss of 0.11 eV if this requirement cannot be fulfilled in a $p(3\times1)$ arrangement. As only subsurface substrate atoms relaxations along [001] are possible at short bridge and top sites, substrate relaxation plays no role for t_{short} and top t_{top}, and is very small for t_{hollow}.

(b) *Barriers*. For short-bridge Br atoms hopping along atop close-packed Pt rows the barrier is 0.35–0.39 eV depending on whether ''single'' or chains (different filling) of Br atoms move [compare Figs. 5(i)–5(l) and 5(a)–5(c)]. Perpendicular to the Pt rows, short-bridge Br atoms would have to cross the most unfavorable hollow sites, yielding a 0.25 eV higher barrier, which can be avoided by traveling via long-bridge sites. Compared to the short-bridge sites, the barriers for long-bridge Br atoms moving via top sites are smaller and depend on the filling of the long-bridge sites. The barrier changes from 0.17 eV (0.28 eV with [001] substrate relaxation) for half filled to 0.04 eV for completely filled long-bridge Br chains [compare Figs. 5(k)–5(l) and 5(b)–5(c)]. It is interesting to note that the barrier along a close packed row (short-bridge to top) is much less sensitive to changes in the local symmetry than the barrier perpendicular to the rows (long bridge to top). Obviously, substrate relaxations around the adsorbate, if allowed by symmetry, facilitate the formation of an optimal Br-Pt bond length. Consequently, if one traces the movement of individual adsorbate atoms, many different local symmetries will be reached and hence also the barriers will be affected. In order to shed some more light on this important aspect, we performed calculations for Br adsorption in a larger $p(4\times3)$ cell. Not quite unexpected we find the barrier along the chain to be 0.35 eV and to change only slightly to 0.34 eV when the substrate is frozen laterally to its bulk (high-symmetry) positions. Perpendicular to the substrate chains, the barriers depend again strongly on possible lateral substrate relaxations which influence mostly the energies in the long-bridge position. Allowing the substrate to relax one finds a barrier of 0.19 eV which almost completely vanishes for high symmetry arrangements, i.e., when the substrate is frozen laterally. This latter result, which should be compared to the 0.28 eV above also clearly shows the sensitivity of the barriers to the number of substrate layers allowing to relax, which had to be restricted to the three top layers in a five layer thick slab, due to computational constraints.

(c) *Repulsions*. The Br-Br repulsion, viewed as the loss of adsorption energy for Br atoms close to already occupied sites, varies in a very characteristic way. It is rather short ranged as can be seen from comparing both Figs. 5(e)–5(h), and Figs. 5(i)–5(m) to Figs. 5(a)–5(d). Thus it is very large for nearest-neighbor occupations along the close-packed [1$\bar{1}$0] Pt rows, in particular, for the short-bridge sites (1.21 eV). Perpendicular to the Pt rows [001] distances are larger, but repulsion is still present showing the largest value for the long-bridge site (0.18 eV or 0.29 eV with substrate relaxation included). In other words, repulsion is larger along bond directions, which is plausible as, on average, fewer substrate states are available per Br-Pt bond when two neighboring Br atoms ''share'' one substrate Pt atom. Figure 6 describes the energy barriers for Br atom movement within a (3×1) structure consisting of rows with every third short-bridge site occupied. The repulsion between short- and long-bridge Br in a (3×1) arrangement is small [0.05 eV, compare Figs. 5(b) and 6(a)]. Long-bridge Br atoms are more or less trapped between the short-bridge Br-Pt chains in the perfect $p(3\times1)$ phase. For them, hopping is only possible perpendicular to the Pt rows, i.e., in the [001] direction. Movement in the [1$\bar{1}$0] direction would imply a passage between two occupied short-bridge sites [Fig. 6(d)], which energetically is extremely unfavorable. In contrast, hopping in [001] direction implies transient occupation of a top site [Fig. 6(g)], which is less demanding energetically. At the same time, the repulsion between neighboring long-bridge sites [Fig. 6(c)] is relieved and therefore, the barrier almost disappears rendering diffusion in this direction facile. Finally we observe that the removal of every second long-bridge Br atom relieves the long-bridge Br-Br repulsion and thereby lowers the energy by 0.14 eV, or—including substrate relaxation—by 0.23 eV [Fig. 6(a) vs Fig. 6(b)].

This analysis provides important insights into the mechanism of the $c(2\times2) \Rightarrow (3\times1)$ phase transition discussed in the following section. Putting an additional Br atom into a short bridge of the $c(2\times2)$ phase (coverage 1/2 ML) would require occupation of neighboring short-bridge sites with an energy cost of about 1.2 eV. This is more than the energy barrier for diffusion, hence a rapid rearrangement of Br atoms around an additional Br ''impurity'' is expected. According to the calculated energies one would predict that long-bridge occupation is introduced to avoid the unfavorable occupation of nearest-neighbor short-bridge sites, but is kept at a minimum, since short-bridge sites are principally

more favorable. Interestingly, this consideration does not apply for $\Theta = 0.5$ ML. Here, a mixed short-bridge/long-bridge (3×2) structure exists which is almost degenerate with the $c(2\times2)$ arrangement [Fig. 6(b)]. The energy difference per Br atom is only $(2\times3.27+3.10)/3-3.25=0.04$ eV. However, increasing the coverage beyond 0.5 ML requires occupation of nearest-neighbor long-bridge sites and hence nucleation of a local (3×1) structure [Fig. 6(c)]. Comparison of Figs. 6(c) and 6(g) indicates that diffusion barriers in a defective (3×1) structure are low and hence rapid dynamics could be expected. At finite temperatures this could yield a considerable entropic contribution to the total free energy of the adsorbate structure, facilitating the transition from the $c(2\times2)$ into the (3×1) phase.

IV. THE TRANSITION $c(2\times2)\Rightarrow(3\times1)$

According to our previous work[9] and that described so far in the present paper the atomic structures of the $c(2\times2)$ and (3×1) phases are reliably resolved for the corresponding ideal coverage in each case, i.e., 1/2 and 2/3, respectively. We now turn to a detailed investigation of the transition regime $1/2<\Theta<2/3$ ML between the two phases. Preparation procedure (i) described above was used, i.e., first a perfect $c(2\times2)$ phase for $\Theta=1/2$ ML was prepared followed by additional Br deposition at $T<190$ K. We will show that there is no continuous compression proceeding from the $c(2\times2)$ to the (3×1) phase. Rather, the $c(2\times2)$ is immediately destroyed and fluctuating (3×1) domains appear within a disordered (1×1) phase as soon as the coverage exceeds 1/2 ML. At small additional coverages, (3×1) antiphase domains are observed. The domain boundaries disappear for $\Theta>0.58$ ML and a globally developed (3×1) phase results. A small additional coverage of NO and CO on the $c(2\times2)$ phase, in contrast, leads almost immediately to a well-developed global (3×1) phase.

A. LEED and STM results

In order to study the emergence of the (3×1) phase when the coverage is increased beyond $\Theta=1/2$ ML, we monitored the variation of LEED beams during additional Br deposition at a fixed primary energy (100 eV). Figure 7(a) compares the evolution of the maximum intensity I_{max} of the (1/2,1/2) spot profile of the $c(2\times2)$ pattern with that for a fractional order spot of the (3×1) phase. Also, the development of the full width at half maximum (FWHM) of the latter spot is included. Clearly, long-range order of the $c(2\times2)$ phase—which focuses intensities into the half-order spot—is rapidly destroyed by additional Br deposition. Simultaneously, intensity is picked up by the third-order spot, but a significant increase is observed only after some induction period, i.e., starting only at about $\Theta\approx0.53$ ML. Immediately above that coverage the growth of I_{max} is consistent with a quadratic coverage dependence up to about 0.58 ML. From there onward the increase seems to have a short linear section but quickly saturates as $\Theta=2/3$ ML is approached. The FWHM of the third-order spot reaches its minimum already at about 0.58 ML.

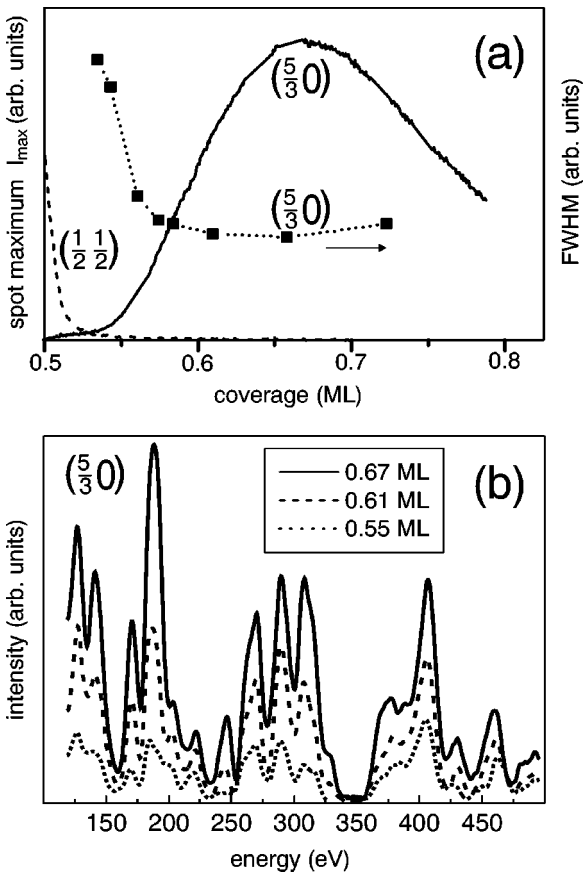

FIG. 7. (a) Maximum intensity of the (5/3,0) LEED spot as a function of Br coverage (solid line), full width at half maximum of the same spot (dotted line with symbols) and maximum intensity of the centered spot in the $c(2\times2)$ pattern of the parent Br/Pt(110) structure (dashed line). (b) LEED $I(E)$ spectra of the (5/3,0) spot for three different Br coverages.

LEED $I(E)$ spectra of the (5/3,0) spot are displayed in Fig. 7(b) for different values of Br coverage. Although the average intensity levels are (and must be) different, the spectral structure of the data is very similar if not identical. Almost every single peak characteristic for the ideal coverage 2/3 ML appears already at 0.55 ML. This indicates that the local structure in developing (3×1) islands is the same as in the perfect (3×1) structure at 2/3 ML coverage from the very beginning of the development. As apparent from the broad beam width [see FWHM curve in Fig. 7(a)] the (3×1) islands at 0.55 ML coverage are still smaller than the transfer width of the LEED optics (typically 100 Å), but their local structure—which determines the integrated intensity[26]—is already the same as in the long-range ordered phase at 2/3 ML coverage.

In this context it is interesting to investigate also the development of integer-order beams. Figure 8(a) displays the spectra of, e.g., the (1,1) beam for the well-ordered $c(2\times2)$ and (3×1) phases at coverage 1/2 and 2/3, respectively. They are substantially different from each other and, in addition, both are markedly different from the spectrum for $\Theta=0.55$ ML given in Fig. 8(b). However, this latter spectrum can be very closely reproduced by a linear super-

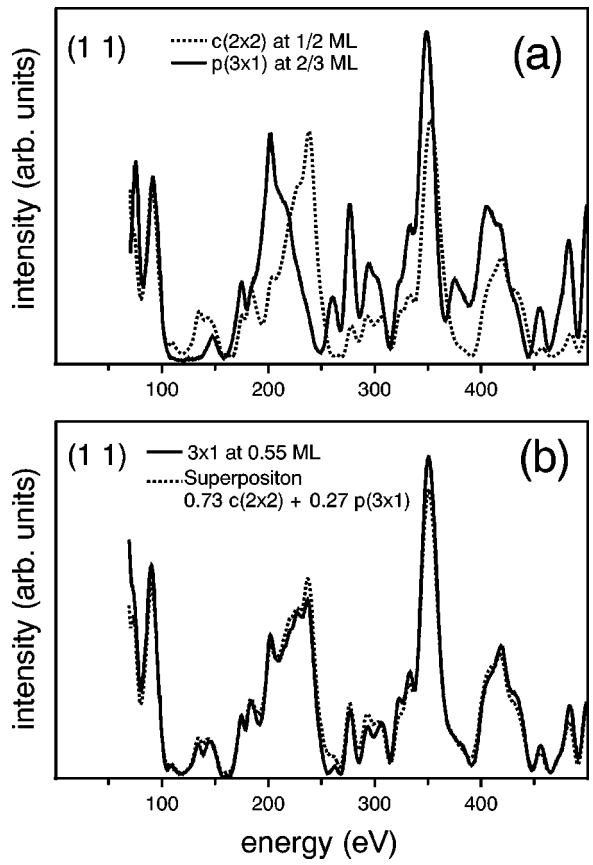

FIG. 8. (a) Spectra of the (1,1) beam for the well-ordered $c(2\times2)$ and (3×1) phases at coverage 1/2 and 2/3, respectively. (b) Spectrum of the (11) beam at coverage 0.55 (full line) fitted by the superposition of the curves displayed in (a).

position of the spectra of the $c(2\times2)$ and (3×1) phases, as is also demonstrated in Fig. 8(b). In addition, the total coverage calculated from the relative weights, i.e., $0.73\times1/2$ ML$+0.27\times2/3$ ML$=0.545$ ML, reproduce the real value (0.55 ML) quantitatively. Spectra at other coverage values between 1/2 and 2/3 ML can be composed equally well whereby the weight of the (3×1) spectrum increases with coverage. In order to understand this behavior, one should note that the spectra of the integer-order beams at 1/2 ML Br coverage are expected to be sensitive to a coverage increase, as new adsorption sites must be populated. Yet, they will be insensitive against the disordering of the $c(2\times2)$ layer, because as long as a local coverage of 0.5 ML is not exceeded the Br atoms in general still occupy every second short-bridge site and thus the local scattering cluster, and presumably also the Pt layer relaxation remains the same.

STM results for selected coverages are shown in Figs. 9(a) and 9(b) for the 0.51 ML and 0.54 ML phases prepared by additional deposition onto the $c(2\times2)$-Br/Pt(110) phase. Figure 9(c) displays the 0.54 ML phase, yet prepared by desorption from a Br layer with higher coverage. Consistent with LEED results the formation of (3×1) islands is observed. It is, however, impossible to determine the extension of the islands from the STM images, because the (3×1) domains exhibit no clearly defined edges. Rather, the intensity modulation in the domains is continuously fading away into areas with a more or less simple (1×1) contrast. Close inspection shows that in the central areas of the (3×1) domains there is always a bright spot centered in the (3×1) unit cell, while in the peripheral regions of the (3×1) domains the structure is essentially of (1×1) type with a (3×1) intensity modulation. The STM results are complemented by the observation that at $\Theta=0.58$ ML a complete global (3×1) structure with a centered (3×1) unit cell is observed [Fig. 1(b)]. Similarly, exposure of the $c(2\times2)$ phase to CO or NO leading to a molecular coverage of ≈0.02 ML also triggers the transition into a (3×1) structure (without any additional Br exposure) with a centered (3×1) unit cell as shown in Fig. 10(a). For comparison, a calculated STM image of the global (3×1) phase at $\Theta=2/3$ ML is shown in Fig. 10(b).

B. Discussion

The LEED results shown in Fig. 7(a) prove that the nucleation of (3×1) islands starts already at a very small increase of the Br coverage above 1/2 ML. Even rather small (3×1) islands own already the same atomic structure as the well-ordered and long-range ordered domains at $\Theta=2/3$ ML. In the coverage range 0.52 ML$<\Theta<$0.58 ML the maximum in the spatial profile of third-order spots, I_{max}, grows approximately as $(\Theta-0.52\ \mathrm{ML})^2$. Such a law is expected for the growth of islands with sizes smaller than the transfer width of the LEED optics (typically 100 Å) and the simultaneous decrease of the spot FWHM supports this interpretation. The transition to an almost linear growth at ≈0.58 ML indicates that the mean island diameter exceeds the transfer width, again consistent with the FWHM, which saturates at about 0.58 ML. In agreement with LEED, the STM images [Fig. 9(a)] show that (3×1) islands are already nucleated at coverage values of 0.51 ML.

Interestingly, the intensities of the half-order beams which are representative for $c(2\times2)$ ordered domains break down quickly, in particular, before third-order beams representative for (3×1) ordered domains gain appreciable weight as displayed in Fig. 7(a). The disappearance of half-order spots mirrors the disappearance of $c(2\times2)$ long-range order, so that constructive interference at half-order spot positions is lacking. Additional to the traces of small $c(2\times2)$ domains preserved and pinned at defects [see Fig. 9(a)] there must be still extended areas with a local coverage of 0.5 as they contribute considerably to integer-order beams as demonstrated in Fig. 8(b). In these areas with 0.5 ML Br coverage, the Br atoms occupy in average every second short-bridge site, but the presence of additional randomly distributed and rapidly moving empty short-bridge sites causes a (1×1) pattern, resulting from time averaging over a fluctuating disordered structure.

Yet, the described LEED observations and interpretations seem to be—at least partially—in contradiction to the STM images. First, the latter show a decreasing strength of the (3×1) modulation as one moves from the center towards the edges of an island. The central corrugation maximum, which is characteristic for the well-ordered phase at coverage 2/3

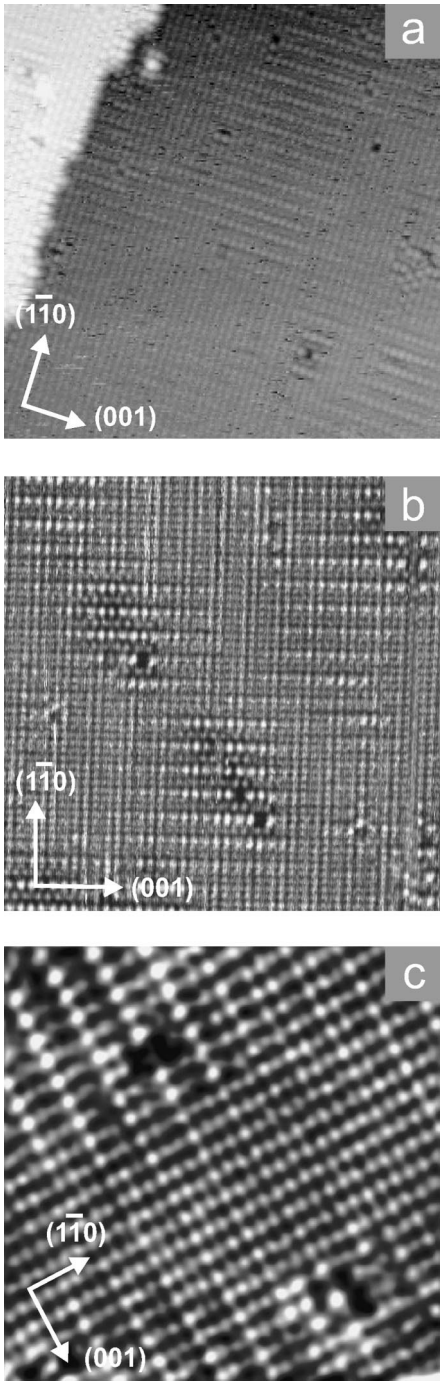

FIG. 9. (a) Constant-current STM image (55 mV, 0.64 nA; 210×210 Å^2) of the $c(2\times2)$ phase with a Br coverage of 0.01 ML additional to 1/2 ML ($\Theta_{tot}=0.51$ ML). The $c(2\times2)$ structure is only preserved close to steps and defects. On the terraces, extended (3×1) domains surrounded by (1×1) disordered areas are visible. (b) Constant-current image (−33 mV, 0.74 nA; 160×160 Å^2) as in (a) but with an additional coverage of 0.04 ML ($\Theta_{tot}=0.54$ ML) dosed onto the $c(2\times2)$-Br/Pt(110) phase. There are three (3×1) antiphase domains. (c) Constant-current image (−17 mV, 0.63 nA; 76×76 Å^2) as in (b) ($\Theta_{tot}=0.54$ ML prepared by thermal desorption from a higher coverage) showing a closeup of the area between adjacent (3×1) domains clearly demonstrating the continuous change in strength of the (3×1) modulation.

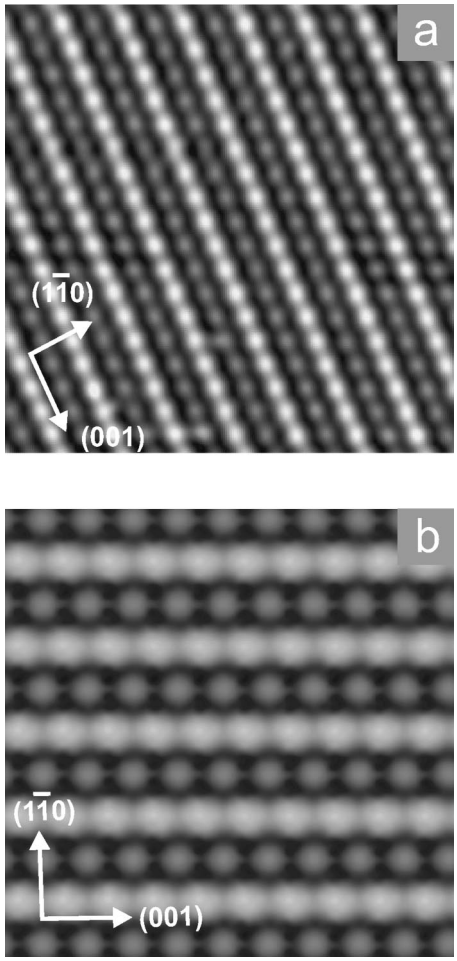

FIG. 10. (a) Constant-current image (−1.28 V, 1.44 nA; 71 ×71 Å^2) of a global (3×1) phase obtained after depositing 0.02 ML of CO onto the $c(2\times2)$-Br/Pt(110) surface. (b) Calculated constant-current image (E_F,E_F+12 meV, Tersoff-Hamann) of a global (3×1) phase at $\Theta=2/3$ ML. Bright spots, Br atoms in short-bridge sites. Darker spots, Br atoms in long-bridge sites.

ML, fades away being compensated by the appearance of two additional maxima between the corner points of the unit cell in $[1\bar{1}0]$ direction. For $\Theta<0.58$ ML it is not even possible to clearly define the edge of a (3×1) domain in the STM image. The different appearance of (3×1) domains in the STM seems to contradict the LEED results which proves that the local structure of the domains is always the same from the very beginning of their development [Fig. 7(b)].

In order to identify the cause of this contrasting behavior it is important to consider the genuine differences of the two experimental methods. A LEED pattern reflects the lateral order of the surface, the integrated intensities of spots stand for the structure of the unit cell with the latter extending into the surface as determined by the electron attenuation length. This includes both Br adatoms and Pt atoms in the first few layers. Lateral disorder is mirrored by the spatial spot intensity profile whereby, e.g., antiphase domains lead to a reduction of the central spot intensity I_{max}. The integrated spot intensity is representative of the number of scatterers in an arrangement with periodicity corresponding to the $\mathbf{k}_\parallel$-vector

of the spot under consideration. If a scatterer fluctuates between different positions, the signal is proportional to the corresponding residence times provided they are, as usual, large compared to the scattering time, which is of the order of 10^{-16} s. In contrast to this LEED scenario, STM ''sees'' only the local density of states. DFT calculations simulating the STM contrast show that in the present case the local protrusion (bright spots in STM) are associated with the Br adatoms. As there are only two types of Br adatoms, i.e., short-bridge and long-bridge adatoms, one should only expect two levels of STM spot intensity [see Fig. 10(b)]. Yet, in Fig. 9 one observes a continuous transition from very bright spots to normal spots in a (1×1)-like arrangement. With the coverage being close to 1/2 ML it is impossible to associate every spot with a Br atom. Attempts to assign the spots partly to Br, partly to Pt atoms are implausible in view of the continuously varying intensity. Also, such a model would yield considerably different LEED intensities. Therefore we interpret the STM spot intensity as a result of time averaging. If the temporal fluctuations are much faster than the time needed by the STM to measure one pixel ($\approx$0.3 ms) the STM image mirrors the time average of the spatial adatom distribution. It is of course possible that the tip-sample interaction influences the temporal fluctuations, but STM scans taken with different tunneling resistance always reveal qualitatively the same structure. In the following section we focus on the issue of fluctuations and their possible relation to a charge-density wave.

V. THE FLUCTUATION MODEL

The most plausible interpretation reconciling the LEED and STM results invokes temporal fluctuations. In this model, additional coverage yielding $\Theta>1/2$ ML leads to nucleation of the (3×1) phase with a local coverage close to the ideal value of 2/3 ML. Initially, most of these nuclei form antiphase domains, which keeps the central intensity I_{max} of the third-order spots small during the nucleation stage. Simultaneous to the nucleation of the (3×1) phase a long-ranged disordering of the $c(2\times2)$ structure takes place and results in a (1×1) LEED pattern, the central spots of the $c(2\times2)$ structure being converted into a streaky background. The disorder is interpreted to arise from the nucleation of (3×1) nuclei. At the phase boundaries of the (3×1) islands vacant sites belonging either to the (3×1) or the $c(2\times2)$ mesh are formed. Br atoms from either phase may hop into those vacancies thus allowing the vacancy to ''evaporate'' from the phase boundary into the neighboring phase. One such process is illustrated in Fig. 11: A Br atom hops out of a short-bridge site within a local $c(2\times2)$ configuration into a long-bridge site belonging to the (3×1) mesh. This creates a vacancy in the $c(2\times2)$ phase, which then travels along the $(1\bar{1}0)$ direction, converting a stripe from a local $c(2\times2)$ into a local (2×1) structure. A few such events can give rise to a complete destruction of the long-range order of the $c(2\times2)$ and the development of a disordered (1×1) structure. Conversely, Br atoms hop from long-bridge sites in the (3×1) mesh into vacant short-bridge sites. With both processes taking place, the (3×1) nuclei may fluctuate locally although their total area remains approximately constant. If the decomposition of the adsorbate layer into local (3×1), $c(2\times2)$, and (2×1) structures would result in a static pattern, it should be detectable in STM images in view of the large corrugation of the Br atoms. Therefore it has to be a dynamical process associated with rapid fluctuations. No (2×1) and $c(2\times2)$ domains are resolvable (apart from the immediate neighborhood of defects). The actual STM contrast is therefore most plausibly explained, if one assumes temporal fluctuations between patches with (3×1) and disordered (1×1) structures. With the fluctuations taking place on a short enough time scale the average tunneling current is proportional to the occupation probability of the corresponding site. Accordingly, the STM images indicate the formation of (3×1) islands with a static central region. This is the area, where a clear (3×1) contrast is observed. At the edges of the islands the Br atoms fluctuate into a disordered (1×1) structure with a local coverage of 0.5 ML. Thus the characteristic corrugation for the (3×1) structure diminishes. Further away from the (3×1) nucleation centers an almost evenly distributed occupation probability for every lattice (short bridge) site is observed. The resulting STM contrast is that of a (1×1) structure. A very weak modulation with threefold periodicity indicates that even far from the center of the (3×1) domains the occupation probability is slightly higher for every third short-bridge site.

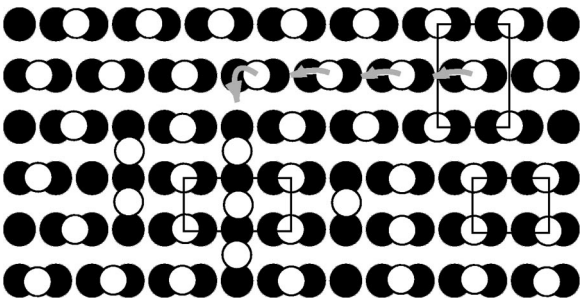

FIG. 11. Ball model of the transition from the $c(2\times2)$ into the (3×1) phase. Black circles are substrate Pt atoms, white balls are Br atoms. In the lower left a (3×1) island is nucleated. At the right side of the island the $c(2\times2)$ structure is locally converted into a $p(2\times1)$ structure. A possible fluctuation process is indicated: One Br atom jumps from a short-bridge site into a long-bridge site thereby augmenting the (3×1) nucleus. The vacancy left behind in the Pt-Br chain may migrate to the right and convert another stripe from a $c(2\times2)$ into a (2×1) structure. With such processes occurring at high frequency every short-bridge site has the same Br occupation probability. The result is a fluctuating disordered (1×1) structure with local coverage 0.5 ML. A (3×1), a (2×1) and a $c(2\times2)$, unit cell are delineated by black rectangles.

This model is supported by temperature-dependent STM measurements[27] on Br/Pt(110) with $\Theta<0.5$ ML. They show a high mobility of the Br atoms along the close-packed Pt atom rows at room temperature. Only for $T<140$ K the Br mobility freezes out. The fluctuation model presented here can also be quantified to some extent by quoting the calculated DFT barriers. Consider for instance the first step of the process illustrated in Fig. 11: It involves a transition from a

$c(2\times2)$ short-bridge site into a long-bridge site. The energy of the former is ≈ 3.25 eV, the energy of the latter can be estimated as 2.92 eV from Fig. 6(c). Thus, this step costs about 0.33 eV (not taking into account energetically more unfavorable transition states). Furthermore, hopping of the resulting vacancy in the $c(2\times2)$ structure along the Pt rows, which creates locally a (2×1) stripe, involves transport of Br atoms across top sites. From Fig. 5(l) the barrier for such a process is estimated to be of the same order (≈ 0.35 eV). Assuming an attempt frequency of 10^{13} s^{-1}, these barriers yield hopping frequencies of the order of 10^{6} s^{-1} at room temperature. A high mobility of the long-bridge Br atoms in [001] direction is expected from the DFT calculations, if there are vacant sites in the long-bridge sublattice. The barrier for such a transport is of the order of 0.04 eV [compare Figs. 5(b), 5(c), and 6(c)]. Although vacant sites in the long-bridge sublattice are energetically favorable [see Fig. 6(b)], the LEED $I(E)$ curves are not consistent with a preferential depletion of the long-bridge sublattice. Rather, they indicate that for coverages exceeding 0.5 ML immediately compact (3×1) islands with local coverage $\Theta_{Br}=2/3$ ML are formed.

So far, following the DFT results we based our discussions mainly on local repulsive interactions. In a previous paper[8] we proposed an alternative explanation to account for the $c(2\times2)\Rightarrow(3\times1)$ phase transition, namely, a Peierls transition into a CDW ground state. This involves an electronic interaction which is localized in **k** space (at $q=2k_F$) and is therefore delocalized (i.e., long range) in real space.

The CDW could stabilize the (3×1) adsorption sites, i.e., every third short-bridge and long-bridge position, thus rendering the (3×1) structure energetically almost degenerate with the $c(2\times2)$ structure. Accordingly, fluctuations between the two structures would result as a natural consequence. The presence of a CDW is actually indicated by the following observations. (i) The formation of a charge-density wave is associated with a spontaneous symmetry breaking, giving rise to a band back folding and opening of a band gap at a position where the undistorted ground state exhibits a Fermi surface. Thus the Fermi surface is removed and the occupied electronic states drop to below E_F. This is precisely what we observe, as shown in Fig. 12 (see also the discussion in Ref. 8). (ii) The (3×1) domains seen in STM (Fig. 9) are not sharply delineated as one would expect for well-defined adsorbate islands. The gradual increase and decrease of the (3×1) corrugation can be attributed to temporal fluctuations. The interaction causing the threefold modulation seems to be long ranged, as expected for a CDW mechanism. (iii) The transition into the (3×1) phase can be triggered by widely different adsorbates, from heavy, strongly bonding Br atoms to light, weakly bonding molecules (NO, CO).[3,7] Both, local bonding as well as direct adsorbate interactions are rather different for these species. Hence it is tempting to attribute the (3×1) structure evolving in both cases to a more general mechanism which depends more on the properties of the parent system than on those of the additional adsorbate. (iv) By definition, a CDW is associated with a periodic lattice distortion which derives from the freezing of a phonon mode. The structure determination by LEED and the independent DFT calculations show a strong vertical periodic modulation in the topmost Pt atom rows, which can be interpreted as a frozen Rayleigh phonon in agreement with a CDW model (Fig. 3). (v) The DFT calculations of the total charge density associated with the various types of Pt atoms within the slab indicate the existence of a charge-density modulation on the topmost atom rows. Within about 1.5 eV below the Fermi level the charge density around the Pt atoms forming short-bridge sites is significantly higher than around the Pt atoms supporting long-bridge sites, although the Br-Pt bond length is almost the same in both cases (Fig. 13). Thus both, the charge density as well as the atomic positions in the Pt substrate are periodically modulated as one would expect for a CDW phase. (vi) The structural changes observed in the adlayer upon shifting the Fermi surface deliberately by adsorbates[3,7] agree with the predictions of theory for a CDW.[6]

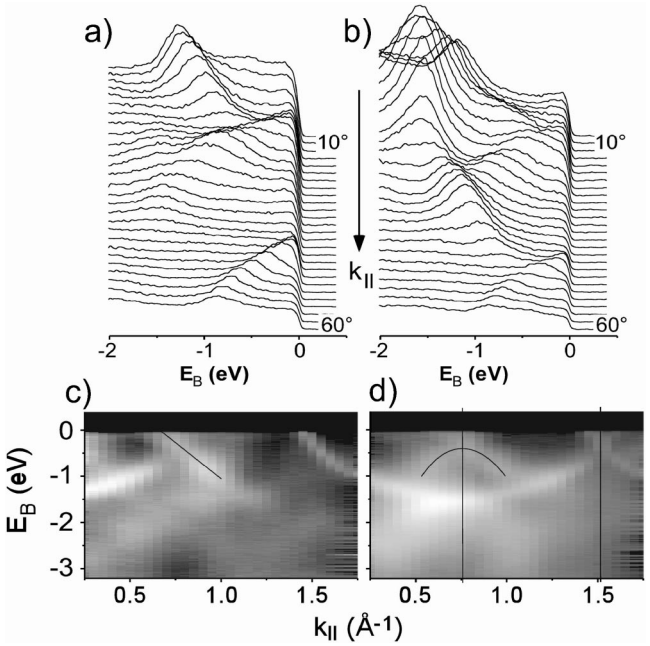

FIG. 12. (a) ARUPS spectra as a function of polar angle obtained on a $c(2\times2)$-Br/Pt(110) surface. $k_{\|}$ points along the Br-Pt chains. (b) A similar series of ARUPS spectra obtained on a (3×1)-Br/Pt(110) surface. (c) Gray-scale image of the spectral intensities observed in (a) plotted over $k_{\|}$. The thin black line serves as a guide to the eye and indicates the dispersion of a surface resonance band. Its crossing with E_F indicates the presence of a Fermi surface generated by this band. (d) Gray-scale image of the spectral intensities observed in (b) plotted over $k_{\|}$. The curved black line indicates the back folding of the band marked in (c). As the band no longer crosses E_F, the Fermi surface has been removed around this point in the SBZ. Vertical black lines show the position of the new surface Brillouin zone centers Γ' and Γ'' in the (3×1) structure (Ref. 28).

The above scenario describes the transition from the $c(2\times2)$ into the (3×1) phase by assuming an energetic stabilization of the (3×1) adsorption site via a CDW. The DFT results, however, are at variance with such an explanation. According to the calculations, the adsorption energy of Br in the long-bridge sites is ≈ 380 meV less favorable than

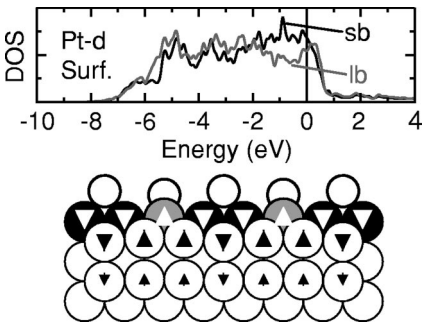

FIG. 13. Top: *d* derived local density-of-states (*d*-LDOS) associated with Pt atoms in the topmost layer. Black line: *d*-LDOS for Pt atoms coordinated to Br in short-bridge sites. Gray line: *d*-LDOS for Pt atoms coordinated to Br in long-bridge sites. Note the charge depletion within states just below the Fermi level for long-bridge Pt atoms. Bottom: Schematic cross section of the (3×1)-Br/Pt(110) surface showing Pt atoms coordinated to Br in short-bridge sites as filled black circles and Pt atoms coordinated to Br in long-bridge sites as filled gray circles. Br atoms are indicated by empty circles on top. The arrows within the Pt atoms indicate the direction of the relaxation relative to the ideal layer spacing of 1.39 Å.

in the short-bridge sites. Population of the (3×1) long-bridge site is, according to DFT, essentially due to the local Br-Br repulsion. Therefore, we have two models to describe the $c(2\times2)\Rightarrow(3\times1)$ phase transition: One is based on the assumption of an energetic stabilization of the (3×1) structure due to a CDW mechanism.

The second model suggested by the DFT calculations emphasizes the role of local repulsive interactions. Here the energy gain resulting from the CDW is not sufficient to pull the (3×1) below the $c(2\times2)$ surface free energy. Hence, formation of the (3×1) phase would not occur without additional local repulsion. The CDW is then facilitating but not driving the phase transition. We call this a CDW-assisted phase transition.

Quantitatively, the energy gain from the $2k_F$ interaction evident in Fig. 12 is clearly smaller than the calculated 0.18 eV total energy difference between the $c(2\times2)$ and the (3×1) structure. Although the electronic states at k_F are lowered by about 0.2 eV, this stabilization is restricted to a small area in *k* space. In principle, there is a gradual transition from weakly-coupled to strongly-coupled CDWs.[29] The former feature a well-defined $2k_F$ interaction, which is long-ranged in real space, the latter involve a much larger set of electronic states with *k* values being spread out significantly around k_F. Accordingly, the interaction is locally more confined in real space for the strong-coupling case. The CDW discussed here is apparently of the weak-coupling type, because the ARUPS results show that the energetic down shift of the electronic states is confined to a narrow region around k_F (see Fig. 12). Furthermore, the STM images show that the (3×1) correlation fade away rather slowly at the edges of the (3×1) domains, indicating a long-range interaction.

We conclude with a word of caution concerning the DFT results. The DFT calculations were extremely successful with respect to predicting the geometric structure. Therefore one would tend to accept the total energy values as quite reliable. However the DFT results were obtained without taking spin-orbit splitting into account. Therefore, they do not correctly represent the Fermi surfaces and the corresponding $2k_F$ interaction. Furthermore, the DFT band structure is difficult to reconcile with the ARUPS results: Angle-resolved photoemission data show pronounced surface state bands, which are not reproduced in the DFT band-structure calculations. In addition, ARUPS reveals strong many-body effects in surface-resonance bands close to E_F,[30] which argues for a considerable electronic correlation. Thus, while DFT calculations may go a far way describing the ground state even of correlated systems, they are of limited value for interpreting photoemission results in such materials.

VI. SUMMARY

The atomic structure of the (3×1)-Br/Pt(110) phase has been determined by quantitative LEED and DFT calculations. While in the $c(2\times2)$-Br/Pt(110) structure every second short-bridge site is occupied, it is only every third short-bridge site in the (3×1) phase. The other half of the Br atoms occupy every third long-bridge site in between. In the $c(2\times2)$ adlayer all Pt atoms in the top layer are coplanar, whereas in the (3×1) phase the Pt atoms forming the Br occupied long-bridge sites are outward relaxed by about 0.23 Å. In the (3×1) structure the Pt substrate bears all the hallmarks of a CDW phase including periodic modulations of the charge density associated with the top Pt atoms. The transition from the $c(2\times2)$ to the (3×1) phase can be triggered by a variety of adsorbate particles and seems to involve critical fluctuations at finite temperature as suggested by a comparison of STM and LEED results. The role of the CDW as compared to the (3×1) repulsive local interactions within the Br adlayer in the total energy balance of the $c(2\times2)\Rightarrow(3\times1)$ phase transition remains to be clarified.

ACKNOWLEDGMENT

This work was supported by the Austrian Science Fund.

*Also at Istituto Nazionale di Fisica della Materia (INFM), Dipartimento di Scienze Fisiche, Universitàdegli Studi di Cagliari I-09124 Cagliari, Italy.

[1] A.R. Bishop, Synthetic Metals **86**, 2203 (1997).
[2] S. Sachdev, Science **288**, 475 (2000).
[3] C. Deisl, K. Swamy, R. Beer, A. Menzel and E. Bertel, J. Phys.: Condens. Matter **14**, 4199 (2002).
[4] G. Grüner, *Density Waves in Solids* (Addison-Wesley, Reading, MA, 1994).
[5] J.M. Carpinelli, H.H. Weitering, E.W. Plummer, and R. Stumpf, Nature (London) **381**, 398 (1996).
[6] P. Bak, Rep. Prog. Phys. **45**, 587 (1982).
[7] K. Swamy, C. Deisl, A. Menzel, R. Beer, S. Penner, and E. Bertel, Phys. Rev. B **65**, 121404(R) (2002).

[8] K. Swamy, A. Menzel, R. Beer, and E. Bertel, Phys. Rev. Lett. **86**, 1299 (2001).
[9] V. Blum, L. Hammer, K. Heinz, C. Franchini, J. Redinger, K. Swamy, C. Deisl, and E. Bertel, Phys. Rev. B **65**, 165408 (2002).
[10] C. Deisl, K. Swamy, S. Penner, and E. Bertel, Phys. Chem. Chem. Phys. **3**, 1213 (2001).
[11] Danish Micro Engineering.
[12] K. Heinz, Rep. Prog. Phys. **58**, 637 (1995).
[13] P. Rous, Prog. Surf. Sci. **39**, 3 (1992).
[14] V. Blum and K. Heinz, Comput. Phys. Commun. **134**, 392 (2001).
[15] M. Kottcke and K. Heinz, Surf. Sci. **376**, 352 (1996).
[16] J. Pendry, J. Phys. C **13**, 937 (1980).
[17] E. Wimmer, H. Krakauer, M. Weinert, and A.J. Freeman, Phys. Rev. B **24**, 864 (1981); M. Weinert, E. Wimmer, and A.J. Freeman, *ibid.* **26**, 4571 (1982).
[18] G. Kresse and J. Furthmüller, Phys. Rev. B **54**, 11 169 (1996), URL: http://cms.mpi.univie.ac.at/vasp/
[19] P.E. Blöchl, Phys. Rev. B **50**, 17 953 (1994).
[20] G. Kresse and D. Joubert, Phys. Rev. B **59**, 1758 (1999).
[21] Y. Wang and J.P. Perdew, Phys. Rev. B **44**, 13 298 (1991).
[22] J.P. Perdew and A. Zunger, Phys. Rev. B **23**, 5048 (1981); D.M. Ceperley and B.J. Alder, Phys. Rev. Lett. **45**, 566 (1980).
[23] S.L. Cunningham, Phys. Rev. B **10**, 4988 (1974).
[24] J. Rundgren, Phys. Rev. B **59**, 5106 (1999).
[25] C. Franchini, Ph.D. thesis, Vienna University of Technology, 2002.
[26] K. Heinz, U. Starke, and F. Bothe, Surf. Sci. **243**, L70 (1991).
[27] K. Swamy and F. Besenbacher (private communication).
[28] Due to matrix element effects, different bands are seen at Γ' and Γ'' in the (3×1) structure. The band at Γ' opens a gap at E_F. The band crossing at Γ'' is due to the band traversing E_F at ~ 1.43 Å^{-1} in the $c(2\times2)$ phase and its (3×1) umklapp. The corresponding gap is not resolved and lies entirely below E_F.
[29] T. Aruga, J. Phys.: Condens. Matter **14**, 8393 (2002).
[30] A. Menzel, R. Beer, and E. Bertel, Phys. Rev. Lett. **89**, 076803 (2002).